The Astrophysical Journal, 997:349 (11pp), 2026 February 1 https://doi.org/10.3847/1538-4357/ae30e3

Periodic 6.7 GHz CH_3OH Maser Emission in G353.273+0.641: First Candidate for a Pulsating High-mass Protostar

Sohta Harajiri[1], Kazuhito Motogi[1,2], Ryota Nakamura[1], Yoshinori Yonekura[3], Yoshihiro Tanabe[2], and Kenta Fujisawa[2]
[1] Graduate School of Sciences and Technology for Innovation, Yamaguchi University, Yoshida 1677-1, Yamaguchi 753-8512, Japan
[2] The Research Institute for Time Studies, Yamaguchi University, Yoshida 1677-1, Yamaguchi 753-8511, Japan
[3] Center for Astronomy, Ibaraki University, 2-1-1 Bunkyo, Mito, Ibaraki 310-8512, Japan
Received 2025 November 17; revised 2025 December 18; accepted 2025 December 21; published 2026 January 30

Abstract

We report on the periodic flux variations in the 6.7 GHz CH_3OH maser associated with the high-mass protostar G353.273+0.641, based on 13 yr of monitoring mainly by the Hitachi 32 m telescope. We identified a periodicity of 309 days based on a nearly complete light curve, with 833 epochs every few days. A strong correlation is found between the maser and the mid-infrared fluxes at 3.4 and 4.6 μm observed by NEOWISE during these periods, suggesting that the maser emission responds to variations in the protostellar luminosity. The average profile of the maser light curve is asymmetric and shows a steep drop in intensity just before the brightening, resembling that of some pulsating variable stars. Assuming a protostellar pulsation as the origin of maser periodicity, the observed period implies a cool and highly bloated, red supergiant-like structure. Such a bloated structure is consistent with a theoretical model of protostellar evolution under high accretion rates. The inferred protostellar parameters are broadly consistent with the theoretical model of pulsational instability during the early phase of high-mass star formation. However, a periodic accretion scenario caused by an unresolved compact protobinary cannot be completely ruled out. Several irregular peaks that deviate from the periodicity may result from episodic accretion phenomena or jet-launching events independent of the protostellar pulsation. Extremely high-resolution imaging with next-generation interferometers such as the ngVLA will provide a conclusive test for both the protostellar pulsation and the binary accretion scenarios.

Unified Astronomy Thesaurus concepts: Interstellar masers (846); Star formation (1569); Massive stars (732); Protostars (1302); Time domain astronomy (2109); Radio astronomy (1338)

1. Introduction

In recent years, high-resolution observations by the Atacama Large Millimeter/submillimeter Array (ALMA) have been revealing the stability of accretion disks around a high-mass protostar (M. T. Beltrán & W. J. de Wit 2016; J. M. Girart et al. 2018; K. Motogi et al. 2019; R. Cesaroni et al. 2025). ALMA has also found several high-mass protobinary systems, some of which are likely formed via disk fragmentation (Y. Zhang et al. 2019), while observational information within 100 au of the central protostar is still limited (T. Hirota et al. 2017; A. Ginsburg et al. 2019, 2023). Class II 6.7 GHz CH_3OH masers, which are commonly associated with the disks and inner envelopes around high-mass protostars, offer a valuable alternative method for studying the innermost accretion activities (A. Sanna et al. 2010; C. Goddi et al. 2011; L. Moscadelli et al. 2011; K. Sugiyama et al. 2014; K. Motogi et al. 2017; R. A. Burns et al. 2023; M. Nakamura et al. 2023). This maser corresponds to the 5_1–6_0A^+ transition (K. M. Menten 1991) and is excited by mid-infrared (MIR) radiation (D. M. Cragg et al. 2005). Because of its radiative pumping nature, the maser flux can vary in response to changes in infrared emission from the host protostar. Therefore, the maser variability is a potential tracer of the variable protostellar luminosity and, consequently, its accretion rate.

Explosive increases in 6.7 GHz CH_3OH maser luminosity have been confirmed in objects such as S255IR-NIRS3 (K. Fujisawa et al. 2015), NGC6334I-MM1 (T. R. Hunter et al. 2017, 2018), G358.9–0.03 (K. Sugiyama et al. 2019), and G24.33+0.14 (T. Hirota et al. 2022). These observations suggest that the increase in CH_3OH maser luminosity is due to the rapid increase of the accretion rate as fragmented gas clumps in the accretion disk fall onto the central star (so-called accretion burst).

On the other hand, over 30 periodically variable 6.7 GHz CH_3OH maser sources have been identified (Y. Tanabe & Y. Yonekura 2024, and references therein; M. Szymczak et al. 2024; P. Wolak et al. 2025). For example, the archetypal object G9.62+0.20 showed periodic and intermittent variations in the maser flux with a period of approximately 243 days (S. Goedhart et al. 2003). This behavior has been explained by the colliding-wind binary (CWB) model, in which the enhanced free–free seed photons produced by colliding stellar winds near the periastron drive the periodic maser variability (D. J. van der Walt 2011). We note that some other models, such as a protobinary interaction (S. Y. Parfenov & A. M. Sobolev 2014) or protostellar pulsation (A. Sanna et al. 2015), are still under consideration, although the CWB model appears most plausible in G9.62+0.20 (D. J. van der Walt et al. 2016). In addition to the models that explain the origin of periodicity, F. Rajabi et al. (2023) and T. Rashidi et al. (2025) proposed that Dicke's superradiance may shape the short, burst-like brightening during each flare.

Although multiple physical origins are discussed for several periodic CH_3OH maser sources, in general, these episodic or periodic variations in maser flux are mostly believed to reflect

Table 1
Observational Summaries

	Hitachi 32m	Yamaguchi 32m
Frequency (MHz)	6664–6672	6664–6672
Bandwidth (MHz)	8	8
Spectral channels	8192	8192
Channel spacing (km s^{-1})	0.044	0.044
Velocity resolution (km s^{-1})	0.13	0.13
On source time (s)	300	300
η_A	0.7	0.6
T_{sys} (K)	25–55	45–65
1σ rms (Jy)	∼0.3	∼0.5

changes in radiation from the protostar and surrounding gas/dust.

The target source in this study, G353.273+0.641 (hereafter G353), is a relatively nearby high-mass protostar in the southern sky (1.7 kpc; T. Neckel 1978; K. Motogi et al. 2016), located at R.A. (J2000.0) = $17^h26^m01^s.59$ and decl. (J2000.0) = $-34°15'14''.9$. The 6.7 GHz CH_3OH masers in G353 have been detected inside the nearly face-on disk within 100 au from the protostar (J. L. Caswell & C. J. Phillips 2008; K. Motogi et al. 2017). S.-M. Song et al. (2025) reported a periodic maser flux variation of ∼ 330 days for this maser based on 710 days of monitoring observations with the Tianma 65 m radio telescope during 2022–2023. In this paper, we report on further detailed analysis of this flux variation, based on 13 yr of monitoring observations conducted with the Hitachi 32 m and Yamaguchi 32 m radio telescopes.

2. Observations

Monitoring observations of the 6.7 GHz CH_3OH maser in G353 were carried out using the Hitachi 32 m radio telescope (Ibaraki University; Y. Yonekura et al. 2016) and the Yamaguchi 32 m radio telescope (Yamaguchi University; K. Fujisawa et al. 2002), in order to investigate the maser flux variations. At the Hitachi radio telescope, monitoring observations began in 2013 January. The observational cadence is once every ∼10 days from the start of the monitoring observations to 2015 August, and once every ∼5 days from 2015 September to the present (2025 May 30). At the Yamaguchi radio telescope, daily observations began in 2024 October. Table 1 shows observational summaries.

Observations at both radio telescopes were conducted using a position-switching method. The OFF position was set to ΔR.A.=+60′ from the G353. The integration time per observation is 5 minutes for both the ON and OFF positions. A single left circular polarization signal was recorded at 64 Mbps (16 megasamples per second with 4 bit sampling) by using a K5/VSSP32 sampler (T. Kondo et al. 2008). The recorded bandwidth is 8 MHz (radio frequency: 6664–6672 MHz), and they are divided into 8192 channels. After moving averaging every three channels, the 1σ rms noise level is ∼ 0.3 Jy for the Hitachi radio telescope and 0.5 Jy for the Yamaguchi radio telescope, with a velocity resolution of ∼ 0.13 km s^{-1}. The half-power beamwidth of the Hitachi radio telescope is ∼4′.6 with better pointing accuracy than ∼30″ (Y. Yonekura et al. 2016). The half-power beamwidth of the Yamaguchi radio telescope is ∼5′.0, and its pointing error is also within ∼30″. Although the impact of these errors on the amplitude is relatively small (less than ∼3%), five-point cross-scan observations were conducted for all measurements with the Yamaguchi telescope to improve data accuracy. Both radio telescopes measured the antenna temperature using the chopper wheel method. We used aperture efficiencies (η_A) of 0.7 for the Hitachi telescope and 0.6 for the Yamaguchi telescope. A comparison of flux densities from simultaneous observations at both radio telescopes showed good agreement within a 3σ range, indicating consistent amplitude calibration between the two telescopes.

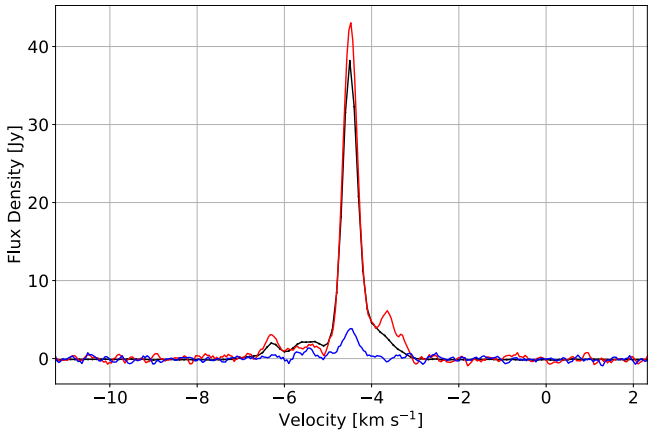

Figure 1. Averaged 6.7 GHz CH_3OH maser spectrum constructed only using channels $\geqslant 3\sigma$ (black). The spectra from the epochs of maximum (red) and minimum (blue) peak flux are also overlaid to show the range of variability.

3. NEOWISE Archival Data

In this study, we utilized archival data obtained by NASA's NEOWISE mission to investigate the relationship between long-term infrared variations and maser flux. NEOWISE is a project that reuses NASA's Wide-field Infrared Survey Explorer (WISE) and has been continuously conducting infrared observations of near-Earth objects since 2013 (A. Mainzer et al. 2014). NEOWISE offers two mid-infrared bands at 3.4 μm (W1 band) and 4.6 μm (W2 band).

We acquired time-series data for G353 from the NEOWISE-R Single Exposure (L1b) Source Table for variability analysis (NEOWISE Team 2020).[4] We set a search radius of 10″ when associating the NEOWISE source with the maser position. The coordinates of the NEOWISE infrared source coincide with the millimeter continuum peak of G353 within 1″. For the photometric data, we applied criteria to ensure reliability: $1\sigma \leqslant 0.1$ mag, signal-to-noise ratio (SNR) $\geqslant 5$, and a high-quality flag of "AA" (ph_qual). Additionally, we averaged all the scans obtained on the same day and adopted the standard error of the mean as the uncertainty. The average and range of the standard errors were 0.30 (0.08–0.75) mag for the W1 band and 0.43 (0.09–1.60) mag for the W2 band.

4. Results

4.1. 6.7 GHz CH_3OH Maser Light Curve

Figure 1 presents the averaged maser spectrum, with spectra at the epochs of maximum and minimum peak flux overlaid to illustrate the range of variability. Here we computed the average flux for each channel only using the data $\geqslant 3\sigma$ from the whole epoch (e.g., M. Felli et al. 2007).

[4] https://irsa.ipac.caltech.edu/data/WISE/docs/release/NEOWISE/

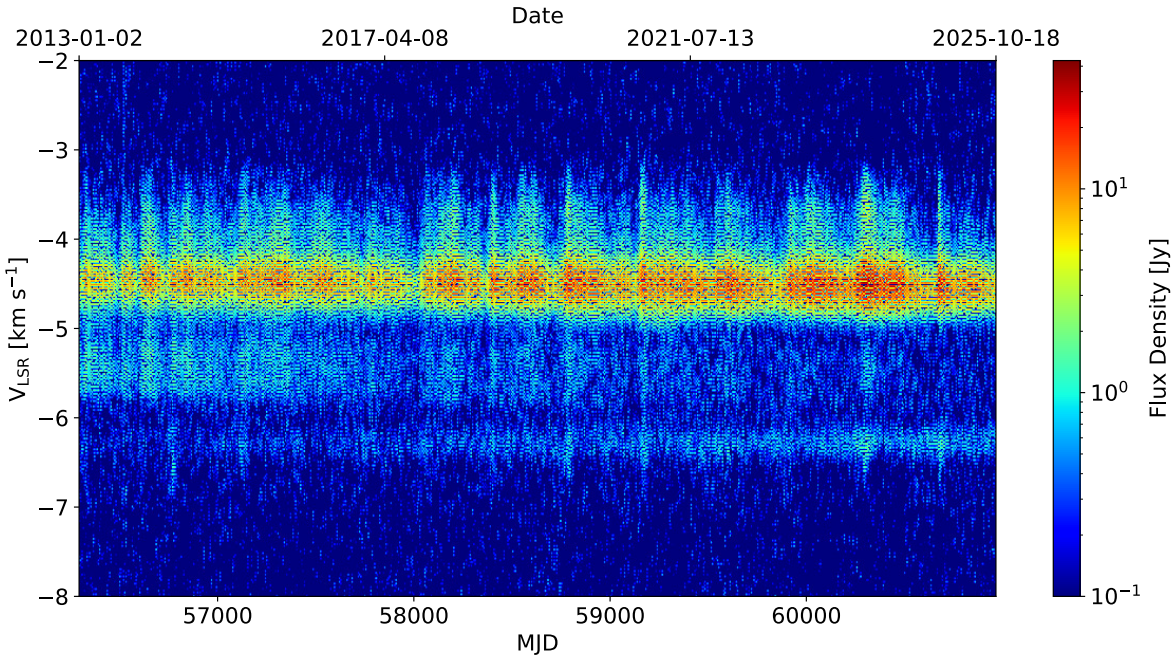

Figure 2. Intensity of the 6.7 GHz CH_3OH maser as a function of local standard of rest (LSR) velocity and modified Julian date of the observations. The plot covers the whole monitoring period. No emission was detected outside the displayed velocity range.

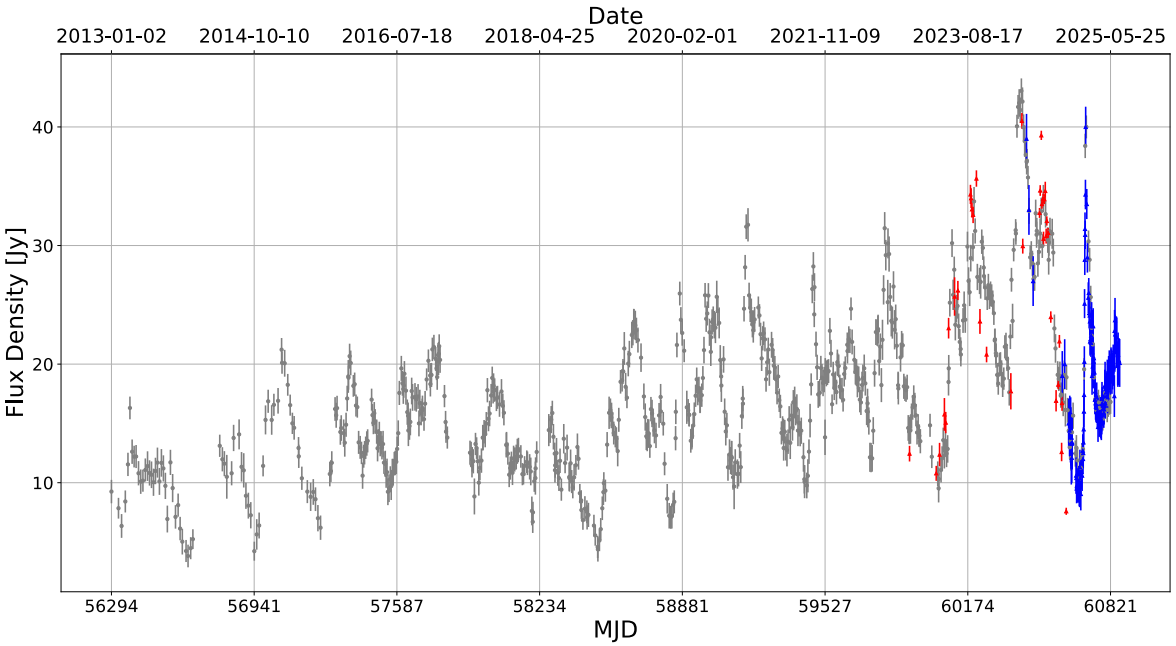

Figure 3. Light curve of the 6.7 GHz CH_3OH maser at $V_{LSR} = -4.5$ km s^{-1} for G353. Gray, blue, and red points represent results from the Hitachi, Yamaguchi, and Tianma telescopes (S.-M. Song et al. 2025), respectively. Error bars indicate the 3σ noise level for each observation.

K. Motogi et al. (2017) conducted observations with the Australia Telescope Compact Array, resolving 43 maser spots and revealing the systematic velocity gradients ($V_{LSR} = -6.5$–3.5 km s^{-1}) along the spatial distribution. The spectrum in Figure 1 also features multiple overlapping components within a similar velocity range. We identified components at $V_{LSR} = -3.7$ and -6.4 km s^{-1}. These two components are the only subpeaks consistently detected over the 13 yr monitoring, while all other subpeaks occasionally appeared. We will also discuss the flux variations of these components along with the main peak later. The component at $V_{LSR} = -5.5$ km s^{-1} was also detected for the first 3 yr, but was later undetectable due to a low SNR (Figure 2). We did not include this component in the following analysis.

Figure 3 shows the light curve of the main velocity component ($V_{LSR} = -4.5$ km s^{-1}). We adopted the peak fluxes derived from Gaussian fitting for the Hitachi and Yamaguchi data. S.-M. Song et al. (2025) conducted 36 epochs over ∼710 days during 2022–2023. They reported a possible periodicity of ∼330 days in the 6.7 GHz CH_3OH maser flux. We also identified a periodic variation of the maser, but the period was shorter than 330 days.

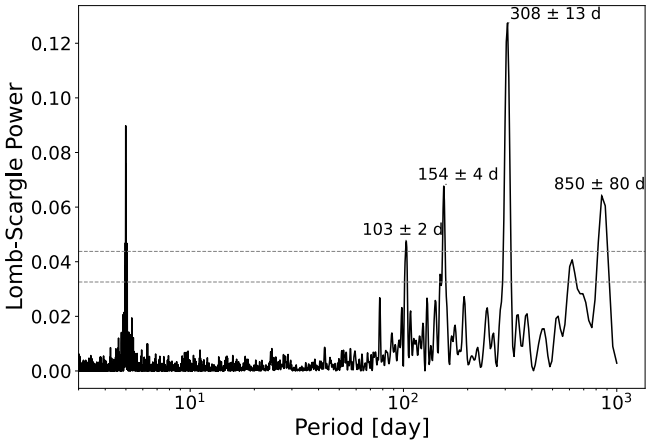

Figure 4. The results of the LS analysis at $V_{\rm LSR}$=−4.5 km s^{-1}. The dashed lines represent the p-values of 0.01 and 0.0001 from the bottom.

4.2. Method of the Period Analysis

To quantitatively evaluate the quasiperiodic light curve in G353, we performed period analysis using the Lomb–Scargle (LS) periodogram method (N. R. Lomb 1976; J. D. Scargle 1982) and the asymmetric power function (APF) fitting (M. Szymczak et al. 2011).

The LS method is suitable for analyzing irregular time-series data. In this study, a period was considered significant when the p-value was less than 0.0001. This hypothesis that the detected period arose by chance corresponds to a confidence level of 99.99% (F. A. M. Frescura et al. 2008). The error of periods obtained by the LS method is estimated as the half width at half-maximum of each peak in the LS power.

The APF used in this study is defined as follows (M. Szymczak et al. 2011; Y. Tanabe & Y. Yonekura 2024):

$$S(t) = A \exp s(t) + Ct + D \tag{1}$$

$$s(t) = \frac{-B\cos\left(2\pi\frac{t}{P} + \phi\right)}{1 - f\sin\left(2\pi\frac{t}{P} + \phi\right)}. \tag{2}$$

Here, A, C, and D are constants; B represents the amplitude to the mean value; P is the period; ϕ is the phase at time $t = 0$; and f represents the asymmetry parameter. The parameter f is the increase time from the minimum to the maximum divided by the period, and it ranges $-1 < f < 1$ (M. Szymczak et al. 2011). In this paper, we consider the function to be symmetric when $-0.5 \leqslant f \leqslant 0.5$, following the definition by Y. Tanabe & Y. Yonekura (2024).

Figure 4 shows the LS power of the peak flux at $V_{\rm LSR}$=−4.5 km s^{-1}. The sharp peak at 5 days was caused by the observation sampling cadence and was excluded because it did not represent a true periodicity. The LS analysis revealed a strong peak at a period of 308 ± 13 days. The APF analysis yielded a period of 309.29 ± 0.23 days, with an asymmetric profile. Although multiple periods (including harmonics of the main peak) were detected, we focused only on the periods identified by both the LS analysis and the APF fitting.

The same analyses were also performed for the velocity components $V_{\rm LSR}$ = −3.7 and −6.4 km s^{-1} identified in Figure 1, with results summarized in Table 2. Figure 5 shows the light curve for each velocity component, overlaid with the fitted APF. In this analysis, the fitting was performed on the entire light curve without amplitude scaling in each cycle, i.e., the model sets the single best-fit amplitude parameter A. Hence, the model does not perfectly match the peak amplitude in each cycle but successfully reproduces the typical shape of the variability profile. The APF profile for the $V_{\rm LSR} = -6.4$ km s^{-1} component is different from the other two, probably due to the limited SNR.

Table 2
Results of Period Analysis

$V_{\rm LSR}$ (km s^{-1})	$P_{\rm LS}$ (days)	$P_{\rm APF}$ (days)	$\lvert f\rvert$
−4.5	308 ± 13	309.29 ± 0.23	0.96
−3.7	308 ± 15	309.28 ± 0.18	0.97
−6.4	312 ± 13	310.97 ± 0.34	0.86

The periods of the −4.5 and −3.7 km s^{-1} components agree with each other within the errors, and their variations are synchronized. In contrast, the period of the −6.4 km s^{-1} component differs by ∼1.5 days from that of the other two components, and this determines a time delay that becomes equal to ∼2 weeks at the end of our monitoring.

The light curve shows a characteristic asymmetric profile with a steep rise and a shallow decay. We regard the rising phase as the beginning of each cycle, i.e., $t = 0$ corresponds to $\phi = 0$ in Equation (2). Irregular brightenings are seen in some cycles that do not align with the established periodicity, as shown in Figure 5.

In addition to the periodic pattern, there is a long-term increasing trend for the $V_{\rm LSR}$ = −4.5 and −6.4 km s^{-1} components. Such a long-term trend is often seen for periodic maser sources (e.g., Y. Tanabe & Y. Yonekura 2024). This may reflect an increasing trend of seed photons for maser amplification, since no such trend was seen in MIR pumping radiation (see next subsection).

Figure 6 shows an enlarged view of the light curve in Figure 3, compared with the results of S.-M. Song et al. (2025). They reported periods of 320 ± 46 days and 331 ± 4 days based on the LS method and APF fitting, respectively. Because of our longer monitoring duration and higher cadence, we could identify the accurate period and APF profile we detected. They treated the primary peak as an outlier in their profile fitting and mistakenly identified a secondary peak as the main one. This secondary peak sometimes appears and is inconsistent with the actual period derived from the LS analysis. We will discuss this subpeak in detail in Section 5.

As a result, both the derived period and the variation profile in S.-M. Song et al. (2025) differed from those obtained in our study. In particular, the asymmetry parameter reported by S.-M. Song et al. (2025) was 0.35, while 0.96 in our case, differing by a factor of approximately three. Therefore, we consider the period of 309 days at $V_{\rm LSR}$ = −4.5 km s^{-1}, obtained from the multiple cycles, as the most reliable. We proceed with our discussions adopting this period. We note that these discrepancies in period and asymmetry parameter do not significantly affect the discussion of thermal CH_3OH emission in S.-M. Song et al. (2025).

4.3. Infrared Archival Data by NEOWISE

Figure 7 compares the light curves of the 6.7 GHz CH_3OH maser and NEOWISE archival data. When comparing the variations of the maser and MIR within each cycle, the

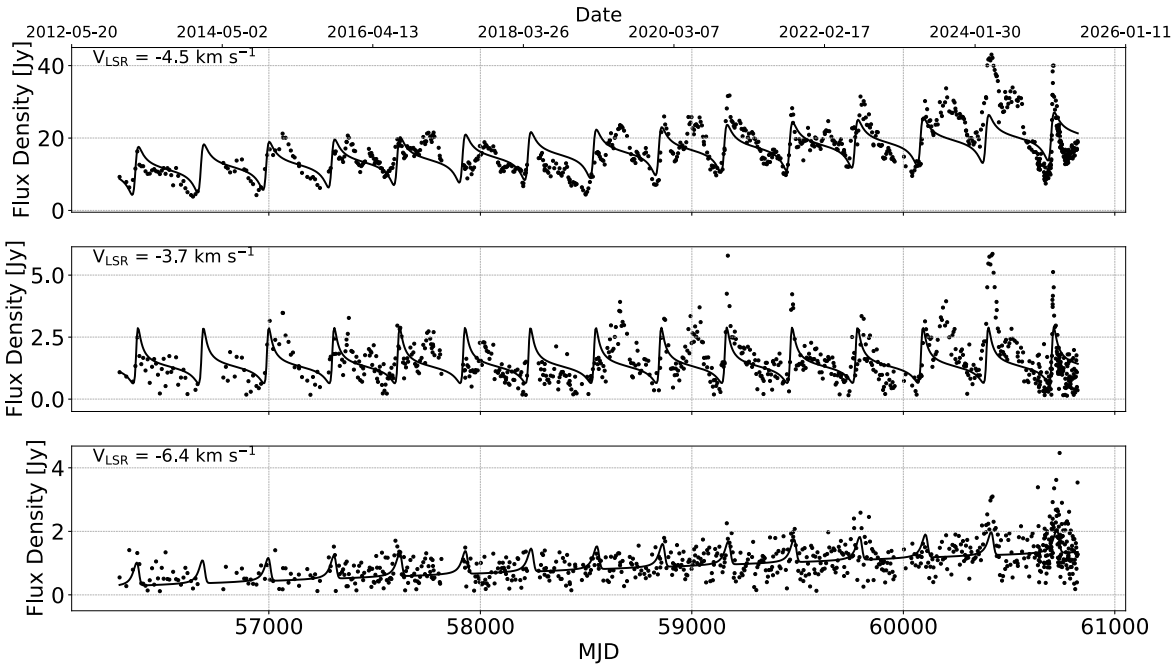

Figure 5. Light curves of the 6.7 GHz CH_3OH maser with the APF overlaid. From top to bottom, the light curves for the velocity components of $V_{LSR} = -4.5$, -3.7, and -6.4 km s^{-1} are shown, respectively.

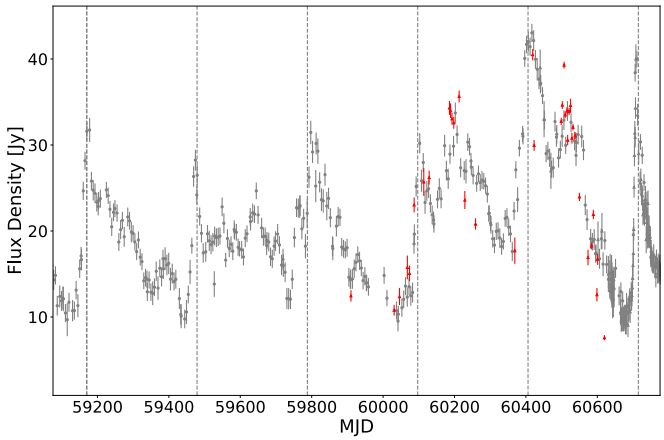

Figure 6. Enlarged view of the light curve shown in Figure 3, focusing on the duration discussed by S.-M. Song et al. (2025). The gray dots represent data from the Hitachi and Yamaguchi radio telescopes, while the red dots represent data from the Tianma telescope. The dashed vertical lines indicate intervals of 309 days, corresponding to the maser cycle.

CH_3OH maser and MIR light curves show consistent trends, that is, a decreasing trend observed in almost all cycles. Figure 8 shows the correlation plots between the flux density of the 6.7 GHz CH_3OH maser and the magnitude of NEOWISE W1 and W2 bands. Each point corresponds to the maser and infrared data observed within ±5 days of each other. The correlation coefficients for W1 and W2 are 0.72 and 0.78, respectively, indicating a positive correlation between the maser and these MIR magnitudes.

5. Discussion

5.1. Origin of 6.7 GHz CH_3OH Maser Periodicity

The theoretical models for periodic variability of 6.7 GHz CH_3OH masers can be categorized into five groups: (1) protostellar pulsation instability (K. Inayoshi et al. 2013), (2) CWB (D. J. van der Walt 2011), (3) eclipsing binary (J. P. Maswanganye et al. 2015), (4) spiral shock (S. Y. Parfenov & A. M. Sobolev 2014), and (5) periodic accretion (P. Artymowicz & S. H. Lubow 1996; D. J. Muñoz & D. Lai 2016). The models (2) to (4) are excluded in G353 for the following reasons. First, G353 does not possess an HII region (K. Motogi et al. 2017), making the CWB model inappropriate, which presupposes the presence of an HII region. Second, G353 possesses a face-on disk. Consequently, the eclipsing binary model and the spiral shock model, both of which require an edge-on disk configuration, are not applicable.

The model (5) is also unlikely, i.e., the periodic accretion model is characterized by recurring bursts and quiescent phases, as shown by observations from E. D. Araya et al. (2010). This behavior is different from that of G353, which has a continuous light-curve profile with no quiescent phase. Moreover, in the interpretation proposed by E. D. Araya et al. (2010), the accretion rate should vary from cycle to cycle, in contrast with the reproducibility of the asymmetric shape of the light curve observed in G353.

Moreover, models (2) to (5) are premised on being caused by binary stars or circumbinary disks. However, as of now, G353 shows no signs of a compact binary system, even in the long-baseline observations by ALMA (spatial resolution ∼20–30 mas, corresponding to ∼ 34–51 au). In contrast, the protostellar pulsation model proposed by K. Inayoshi et al. (2013) can consistently explain the periodic variability observed in G353 (see later discussions).

The superradiance scenario proposed by T. Rashidi et al. (2025) also explains burst-like brightening. It could produce a dip-like profile in some cases (F. Rajabi et al. 2023). However, this model predicts velocity-dependent differences in flare duration, but no clear differences are observed in our data. In addition, the dip-like feature appears after the flare in this model, contrary to the case of G353. Therefore, the present data do not match the superradiance model.

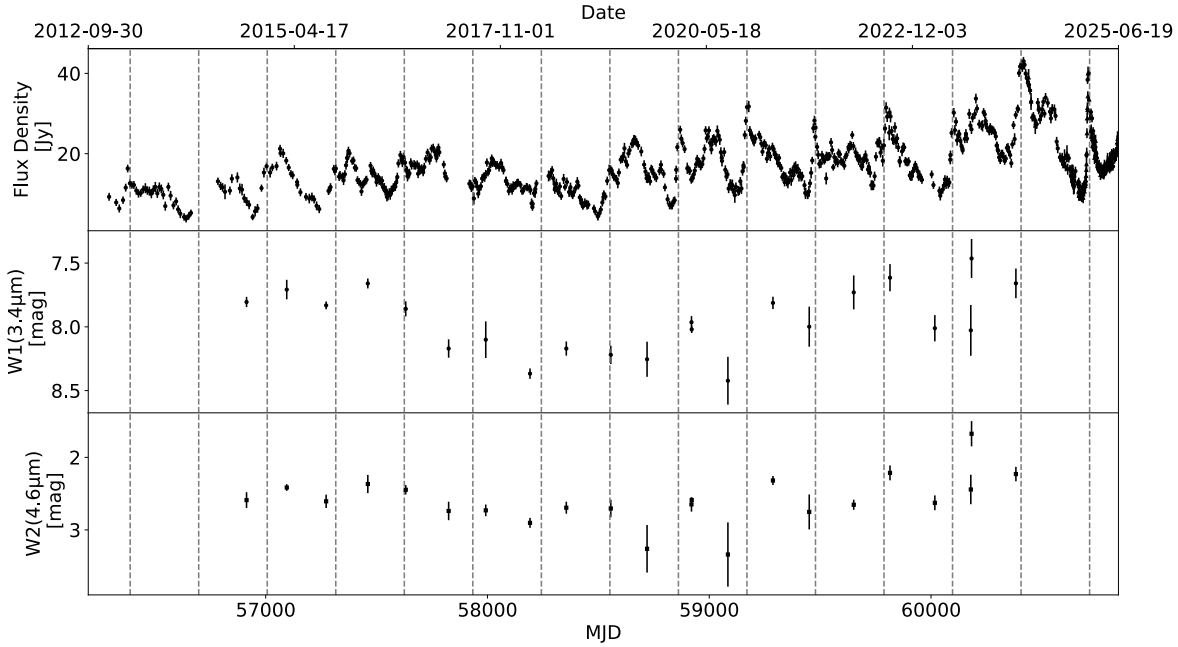

Figure 7. Comparison of the light curves between the 6.7 GHz CH_3OH maser at -4.5 km s^{-1} and two NEOWISE bands. Error bars show 3σ noise level for the maser and standard error for the infrared data. The dashed vertical lines indicate intervals of 309 days.

5.2. Correlated Variability between MIR and Maser

We confirmed a time-series correlation between the MIR and CH_3OH maser emission in G353, as shown in Figure 8. M. Uchiyama et al. (2022) reported a similar correlation between the NEOWISE data and the 6.7 GHz CH_3OH maser flux in a high-mass protostar G036.70+00.09. It is the first confirmation of a MIR–maser correlation in a periodic 6.7 GHz CH_3OH maser source, while such a correlation has previously been reported as a transient phenomenon associated with the accretion burst in S255-NIRS3 (A. Caratti o Garatti et al. 2017). M. Durjasz et al. (2019) also reported a strong MIR–maser correlation for a highly variable but nonperiodic 6.7 GHz CH_3OH maser source.

Such correlations are expected from the well-known IR pumping model in D. M. Cragg et al. (2005), and a statistical trend that Class II CH_3OH maser luminosity correlates with bolometric luminosity (e.g., A. Bartkiewicz et al. 2014; B. M. Jones et al. 2020). In addition to the standard pumping model assuming the MIR reemission by heated dusts, I. I. Zinchenko et al. (2025) have recently reported that direct MIR radiation from the host protostar can excite some class II CH_3OH masers at a millimeter band. Such a direct excitation can also be applicable for the 6.7 GHz CH_3OH maser in principle.

The light curve of the CH_3OH maser in G353 reflects the variability of the protostellar luminosity directly, rather than flux variations of the maser seed photons. The protostellar pulsation model naturally explains such a periodic variation in the (mid-)IR luminosity.

5.3. Maser Variation Profiles for Each Cycle

A detailed profile of a light curve provides an important clue to discuss the physical origin of the periodicity. This fact suggests the involvement of multiple factors in the CH_3OH maser variability of G353.

In Figures 9(a) and (b), the black line displays the typical profile constructed by averaging a normalized profile for each period at $V_{\rm LSR} = -4.5$ and $V_{\rm LSR} = -3.7$ km s^{-1}, excluding five cycles that show clear secondary peaks in their light curves. The red line, which represents the APF obtained in Section 4.2, is overlaid, confirming the shape of the averaged profile. Figures 9(c) and (d) show examples of a light curve of pulsating variable stars, specifically RR Lyrae and Anomalous Cepheids (I. Soszyński et al. 2017). The averaged profile of G353 exhibits good agreement with these characteristic light curves of pulsating variable stars. Furthermore, the amplitudes of maser variation are comparable to those found in such stars.

A particularly noteworthy feature of the averaged light curve is the steep drop in intensity, which is observed immediately before brightening. We highlight this feature by the dashed rectangle in Figures 9(a) and (b). Hereafter, we simply call this feature a dip. Such a dip feature is seen in the light curve of some pulsating variables, as in Figures 9(c) and (d). This feature is thought to arise from a stellar internal ionization region that controls the energy transport process via convection (G. Bono & R. F. Stellingwerf 1994). Although it remains unclear whether the internal structure of the protostar truly matches that of pulsating variable stars, the dip in the light curve is at least distinct from a simple exponential cooling following a nonsteady heating process such as periodic accretion (L. Francis et al. 2022). Therefore, we suggest that the observed dip structure is an indicative sign supporting the hypothesis that G353 is undergoing protostellar pulsation.

5.4. Physical Parameters: Assuming Pulsation Instability

If the periodic pulsation of the protostar itself is the primary cause of the CH_3OH maser variability observed in G353, we can deduce several protostellar parameters based on theoretical models. K. Inayoshi et al. (2013) proposed that protostars become pulsationally unstable during the pre-main-sequence expansion phase. In this pulsationally unstable state, the periodic variation in protostellar luminosity causes the

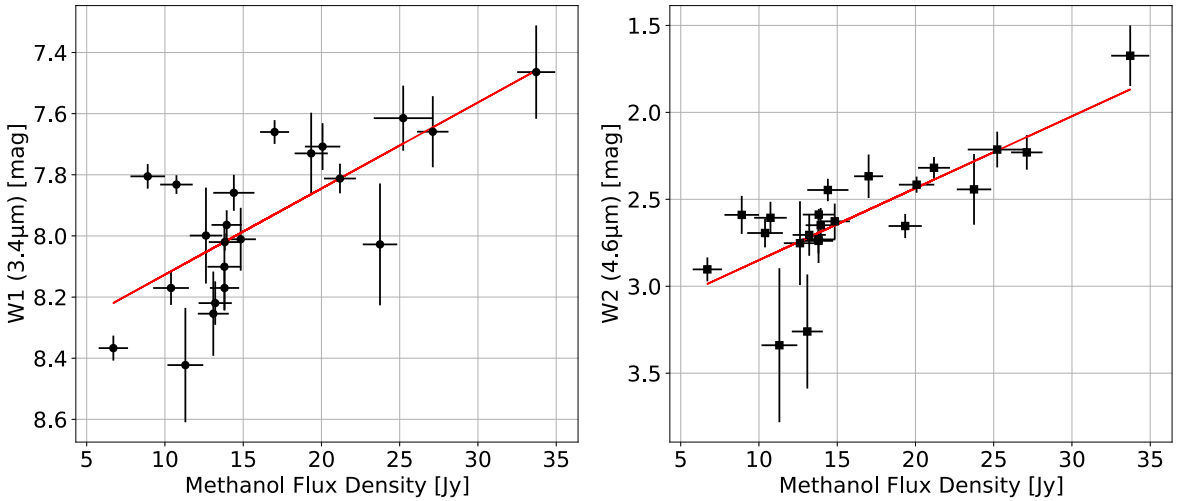

Figure 8. Correlation plots between the 6.7 GHz CH_3OH maser flux density and the NEOWISE W1 and W2 band magnitudes. Error bars are given in the same definition as Figure 7. The red line represents a linear fit by the least-squares method.

temperature of the surrounding dust also to vary periodically, leading to a periodic change in the maser flux. The pulsation timescale of a protostar can be estimated by the freefall time, $t_{\rm ff} \sim \sqrt{1/G\rho}$. Substituting the observed period of 309 days, the expected density is $\sim 2 \times 10^{-5}\,{\rm kg\,m^{-3}}$($\sim 6 \times 10^{15}\,{\rm cm^{-3}}$ in number density). The protostellar mass of G353 is estimated to be $\sim 10\,M_\odot$ from its luminosity (K. Motogi et al. 2017). A simple calculation yields a protostellar radius of $880\,R_\odot$ from an averaged density. This suggests a highly extended, red supergiant(RSG)-like atmospheric structure. Such extended stars typically have a density gradient, with density decreasing exponentially with radius. When applying the typical density gradient of an RSG, it has been reported that the density of most of the stellar atmosphere is about 20% of an averaged density (A. Kozyreva et al. 2020). Considering this, the radius of G353 would be $\sim 500 R_\odot$.

Meanwhile, K. Inayoshi et al. (2013) proposed the following equations to estimate the protostar's radius, mass accretion rate, and luminosity from the variability period:

$$R_* = 350 \quad R_\odot \left(\frac{P}{100\ {\rm days}}\right)^{0.62}, \tag{3}$$

$$\dot{M}_* = 3.1 \times 10^{-3} \quad M_\odot {\rm yr}^{-1} \left(\frac{P}{100\ {\rm days}}\right)^{0.73}, \tag{4}$$

$$\log_{10}\left(\frac{L_*}{L_\odot}\right) = 4.62 + 0.98 \log_{10}\left(\frac{P}{100\ {\rm days}}\right). \tag{5}$$

Table 3 summarizes the results calculated by substituting the period in these equations. For the observed values, the mass accretion rate is adopted from K. Motogi et al. (2019), while the protostellar luminosity values are taken from K. Motogi et al. (2017) and J. S. Urquhart et al. (2022). Regarding the mass accretion rate, the observed value of $3 \times 10^{-3} M_\odot {\rm yr}^{-1}$ obtained by K. Motogi et al. (2019) is consistent with the pulsation model within a factor of 2. The protostellar radius also agrees with the rough estimation based on the freefall time. The protostellar luminosity shows a significant difference, being approximately 20 times higher than the minimum estimate of $5500 L_\odot$ (K. Motogi et al. 2017). Although there is some deviation in the reported luminosities depending on the spectral energy distribution (SED) model, the luminosity is still 1 order of magnitude lower than the theoretical model, even for the most luminous estimate ($14000\,L_\odot$).

This pulsation model is calculated based on the spherically symmetric accretion condition by T. Hosokawa & K. Omukai (2009). It has been pointed out that even with the same accretion rate, the maximum expansion radius of a protostar can differ significantly depending on the initial entropy distribution (S. W. Stahler et al. 1980a; S. W. Stahler et al. 1980b; L. Haemmerlé et al. 2016). S.-M. Song et al. (2025) proposed that high-mass protostars in earlier evolutionary stages tend to exhibit lower luminosity than expected from models in their period–luminosity relation based on a statistical study. Figure 10 presents the period–luminosity relation of periodically variable CH_3OH maser sources statistically analyzed by S.-M. Song et al. (2025). G353 is located significantly below the luminosity predicted by the theoretical equation of K. Inayoshi et al. (2013), but it generally aligns with the linear fit for the lower group, which is considered to be in an early evolutionary stage.

We calculated a protostellar surface temperature for the three luminosity estimations (5500, 14,000 $L_\odot$) by using the Stefan–Boltzmann law. The estimated effective temperatures are $T_{\rm eff} = 2200$ and 2800 K, respectively. Here, we subtracted the accretion luminosity ($L_{\rm acc} \sim GM\dot{M}/R$) from the total luminosities, assuming the observed accretion rate. These low temperatures could imply a cool protostellar atmosphere due to its remarkably expanded radius (D. M. A. Meyer et al. 2019).

5.5. Irregular Brightening Features

We consider that protostellar pulsation can explain most of the features of the maser periodicity in G353. On the other hand, the irregular brightening events that do not align with the cycle could be caused by nonperiodic phenomena independent of protostellar pulsation. For example, episodic accretion events and/or episodic jet-driving events can happen. The unstable accretion disk reported by K. Motogi et al. (2019) implies that the episodic accretion potentially occurs in G353. Moreover, episodic jet activity has also been reported in G353 at intervals of 1–2 yr (K. Motogi et al. 2016). Such a jet-driving event can, for instance, be accompanied by brightening due to shock heating. Alternatively, variations in the infrared optical depth near the protostar due to uplifted gas/dust can

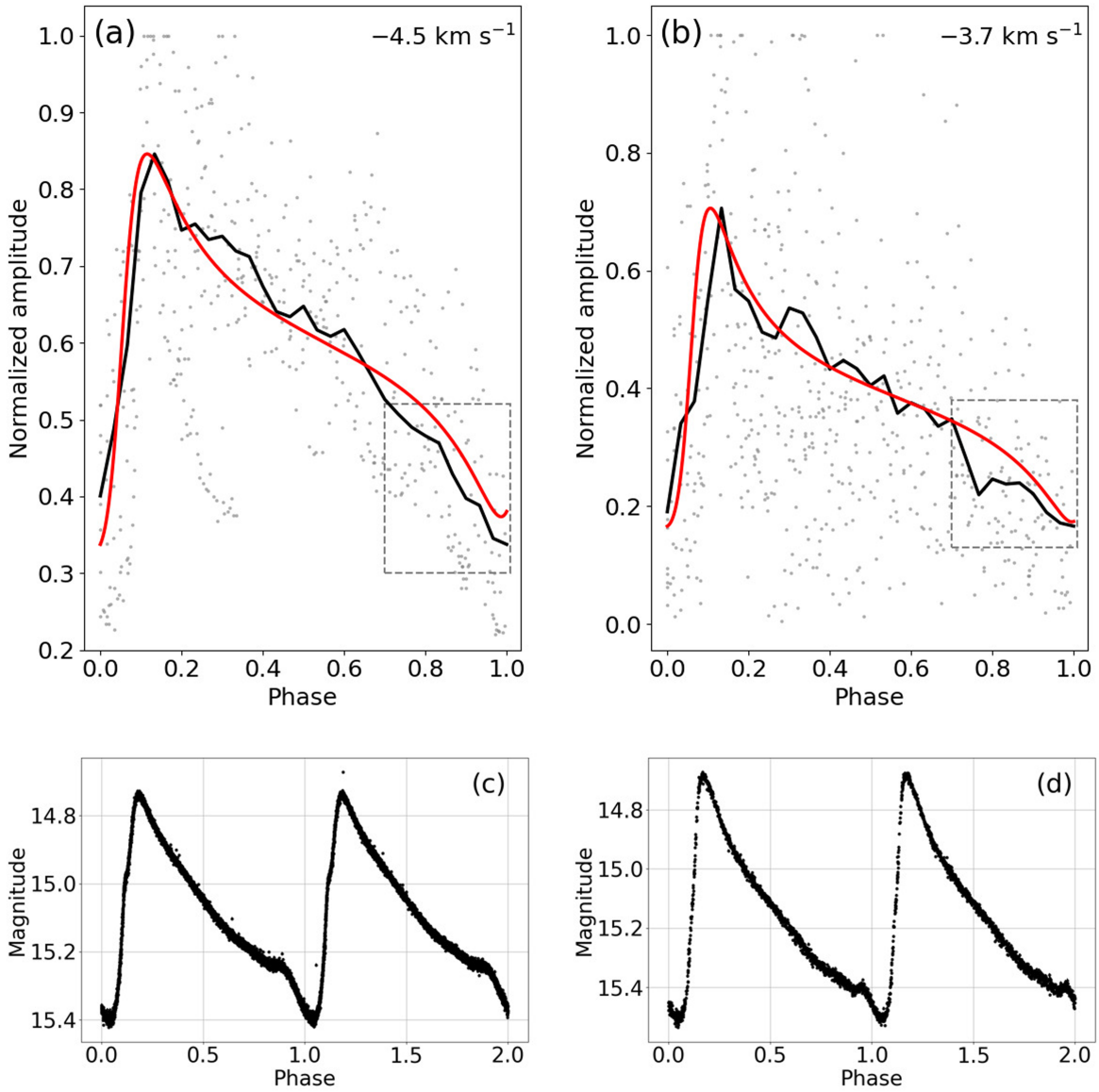

Figure 9. (a) and (b): Black line displays the averaged profiles of the light curve at $V_{\rm LSR} = -4.5$ and $V_{\rm LSR} = -3.7$ km s^{-1}. We calculated the average for every phase bin of 0.03 in each period. The red line shows the overlaid asymmetric power function (APF) obtained in Section 4.2. Gray points represent the original data points before averaging. The dashed rectangle roughly indicates the phase range displaying the steep drop in intensity. (c) and (d) show examples of a light curve for RR Lyrae and Anomalous Cepheids at I band, respectively (I. Soszyński et al. 2017). These are folded and overlaid for every two periods.

Table 3
Protostellar Parameters of G353 Derived from $t_{\rm ff}$ and Pulsation Models

Method	Mass Accretion Rate ($M_\odot$yr^{-1})	Radius ($R_\odot$)	Luminosity ($L_\odot$)
Estimation with $t_{\rm ff}$	...	500	...
Pulsation Model	6×10^{-3}	700	10^5
Observed Values	3×10^{-3}	...	>5500, 14,000

also cause apparent luminosity variations. Simultaneous monitoring observations of the CH_3OH and H_2O maser will allow us to verify the relationship between the irregular peaks and such jet activity.

5.6. Another Remaining Possibility: Protobinary Scenario

Although the pulsation model would successfully explain observed features, we cannot rule out the periodic accretion scenario caused by an unresolved protobinary as the origin of maser periodicity entirely. If we assume a protobinary scenario, certain observational constraints must be satisfied. First, the association of a Class II 6.7 GHz CH_3OH maser and the high bolometric luminosity requires that at least a part of the protobinary is a high-mass protostar. Second, the total mass of the protobinary system must be consistent with the observed bolometric luminosity. Third, given that G353 has a face-on geometry, orbital eccentricity is required to produce the observed periodicity. Such an eccentric binary interacts only at the periastron, producing an adequate time interval. The allowable total mass of the binary system is not uniquely constrained, since the estimated luminosities of G353 varied by a factor of 2 depending on the adopted SED models. In this study, we consider two representative model cases: the protobinary system consisting of 10 and 1 $M_\odot$ objects, and the equal-mass protobinary with two 8 $M_\odot$ objects.

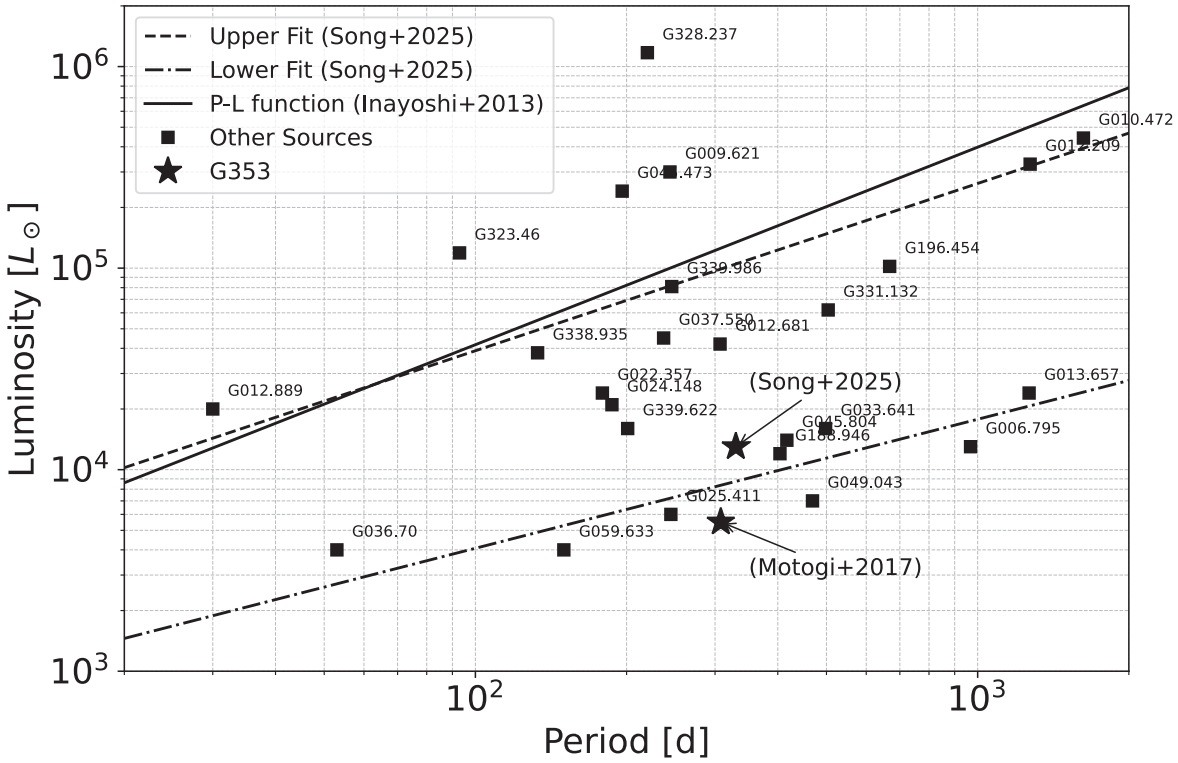

Figure 10. Period–luminosity relation of periodically variable 6.7 GHz CH_3OH maser sources analyzed by S.-M. Song et al. (2025). Black squares indicate the periodically variable maser sources, with the star representing G353. Luminosity values from S.-M. Song et al. (2025) and K. Motogi et al. (2017) are plotted separately due to the difference in luminosity. The black solid line represents the PL function from K. Inayoshi et al. (2013), while the dotted lines indicate linear fits for the upper and lower groups derived by S.-M. Song et al. (2025).

Table 4
Binary Parameters and Angular Separations for Two Modeled Systems

Orbital Phase		10 $M_\odot$: 1 $M_\odot$			8 $M_\odot$: 8 $M_\odot$		
		$e = 0.3$	$e = 0.5$	$e = 0.7$	$e = 0.3$	$e = 0.5$	$e = 0.7$
Periastron	Separation (au)	1.39	0.99	0.60	2.59	1.13	0.68
	Angular separation (mas)	0.82	0.58	0.35	1.52	0.66	0.40
Apastron	Separation (au)	1.58	2.98	3.38	2.93	3.38	3.83
	Angular separation (mas)	0.93	1.75	1.99	1.72	1.99	2.25

For each case, we assumed a plausible eccentricity and calculated the angular separations (Table 4). These calculations assumed a distance of 1.7 kpc. The calculated binary separations at apastron correspond to angular distances of 0.93–2.25 mas. These values are below the highest resolution of ALMA (10–20 mas at Band 6, ∼5 mas at Band 10; ALMA Partnership et al. 2015), making it impossible to resolve the binary separation. In the case of the equal-mass binary (or an adequately bright companion), we may identify phase-dependent shifts in the brightness profile within a synthesized beam along the orbital phase. It may provide an indirect signature of the protobinary if we measure such a sub-beam structure.

The next-generation Very Large Array (ngVLA) is expected to achieve angular resolutions of about 1 mas and brightness temperature sensitivities of several thousand kelvin in the 27–93 GHz band at 7σ or better SNR (R. J. Selina et al. 2018). This extreme sensitivity and resolution will enable us to resolve a protobinary at apastron directly. On the other hand, if G353 is really a pulsating RSG-like protostar with a radius of $\sim 500\,R_\odot$ (diameter ∼4.6 au), its angular size would be about 2.7 mas, allowing for the potential of direct imaging of the protostellar radio photosphere (K. E. I. Tanaka et al. 2021). We are convinced that future high-resolution observations with ngVLA will provide a direct and conclusive confirmation of whether G353 is a single bloated protostar or a protobinary system.

6. Conclusions

We conducted a long-term monitoring observation of the 6.7 GHz CH_3OH maser associated with the high-mass protostar G353 using the Hitachi and Yamaguchi 32 m radio telescopes. We detected significant flux variations with a periodicity of ∼309 days. While several models have been proposed to explain the periodic variability of 6.7 GHz CH_3OH masers, the absence of a HII region and the presence of the face-on disk in G353 exclude most models involving binary interaction or circumbinary disks.

Archival NEOWISE data revealed a positive correlation between the variations of the maser and MIR emission at 3.4 and 4.6 μm. This fact indicates that variations in MIR pumping radiation cause maser flux variations, likely reflecting the variable protostellar luminosity. The average light-curve

profile shows the dip just before the luminosity rise, which is a characteristic feature seen in some of the pulsating variable stars. With these facts, we propose that the protostellar pulsation model is a plausible explanation for the observed maser periodicity in G353.

Based on this, the protostellar density estimated from the freefall timescale is $\sim 2 \times 10^{-5} \mathrm{kg\,m^{-3}}$, with a protostellar radius of about $500\,R_{\odot}$. This radius is broadly consistent with protostellar parameters predicted by the theoretical model proposed by K. Inayoshi et al. (2013). Only the observed luminosity significantly differs from the theoretical prediction, which may be explained if G353 has a larger radius and a cooler atmosphere than the model assumed. Additionally, there were several irregular subpeaks in the light curve, which could be caused by nonsteady accretion events or jet activity independent of the protostellar pulsation.

Another explanation for the maser periodicity via the periodic accretion caused by an unresolved compact protobinary. Although no signature of such a protobinary has yet been identified with ALMA, we cannot completely rule out this scenario at present. Extremely high-resolution imaging with next-generation interferometers such as the ngVLA will allow us to directly resolve a possible protobinary or radio photosphere of a bloated protostar. It will provide direct and conclusive confirmation of the protostellar pulsation scenario.

Acknowledgments

We appreciate the anonymous referee's fruitful comments and suggestions. This work is partially supported by the Inter-university collaborative project "Japanese VLBI Network (JVN)" of NAOJ and by the Japan Society for the Promotion of Science (JSPS) KAKENHI grant Nos. JP21H01120 and JP21H00032. This publication makes use of data products from the Near-Earth Object Wide-field Infrared Survey Explorer (NEOWISE), which is a joint project of the Jet Propulsion Laboratory/California Institute of Technology and the University of California, Los Angeles. NEOWISE is funded by the National Aeronautics and Space Administration. This research has made use of the NASA/IPAC Infrared Science Archive (IRSA), which is operated by the California Institute of Technology, under contract with the National Aeronautics and Space Administration. The archival IRSA services and data include the NEOWISE-R Single Exposure table (NEOWISE Team 2020).

Software: Matplotlib (J. D. Hunter 2007), Numpy (C. R. Harris et al. 2020), Astropy (Astropy Collaboration et al. 2022).

ORCID iDs

Kazuhito Motogi https://orcid.org/0000-0002-3789-770X
Yoshinori Yonekura https://orcid.org/0000-0001-5615-5464
Yoshihiro Tanabe https://orcid.org/0000-0002-1183-7899
Kenta Fujisawa https://orcid.org/0009-0008-1070-4411

References

ALMA Partnership, Brogan, C. L., Pérez, L. M., et al. 2015, ApJL, 808, L3
Araya, E. D., Hofner, P., Goss, W. M., et al. 2010, ApJL, 717, L133
Artymowicz, P., & Lubow, S. H. 1996, ApJL, 467, L77
Astropy Collaboration, Price-Whelan, A. M., Lim, P. L., et al. 2022, ApJ, 935, 167
Bartkiewicz, A., Szymczak, M., & van Langevelde, H. J. 2014, A&A, 564, A110
Beltrán, M. T., & de Wit, W. J. 2016, A&ARv, 24, 6
Bono, G., & Stellingwerf, R. F. 1994, ApJS, 93, 233
Burns, R. A., Uno, Y., Sakai, N., et al. 2023, NatAs, 7, 557
Caratti o Garatti, A., Stecklum, B., Garcia Lopez, R., et al. 2017, NatPh, 13, 276
Caswell, J. L., & Phillips, C. J. 2008, MNRAS, 386, 1521
Cesaroni, R., Galli, D., Padovani, M., Rivilla, V. M., & Sánchez-Monge, Á. 2025, A&A, 693, A76
Cragg, D. M., Sobolev, A. M., & Godfrey, P. D. 2005, MNRAS, 360, 533
Durjasz, M., Szymczak, M., & Olech, M. 2019, MNRAS, 485, 777
Felli, M., Brand, J., Cesaroni, R., et al. 2007, A&A, 476, 373
Francis, L., Johnstone, D., Lee, J.-E., et al. 2022, ApJ, 937, 29
Frescura, F. A. M., Engelbrecht, C. A., & Frank, B. S. 2008, MNRAS, 388, 1693
Fujisawa, K., Mashiyama, H., Shimoikura, T., & Kawaguchi, N. 2002, in 8th Asian-Pacific Regional Meeting, 2, ed. S. Ikeuchi, J. Hearnshaw, & T. Hanawa (Astronomical Soc. Japan), 3
Fujisawa, K., Yonekura, Y., Sugiyama, K., et al. 2015, ATel, 8286
Ginsburg, A., McGuire, B., Plambeck, R., et al. 2019, ApJ, 872, 54
Ginsburg, A., McGuire, B. A., Sanhueza, P., et al. 2023, ApJ, 942, 66
Girart, J. M., Fernández-López, M., Li, Z. Y., et al. 2018, ApJL, 856, L27
Goddi, C., Moscadelli, L., & Sanna, A. 2011, A&A, 535, L8
Goedhart, S., Gaylard, M. J., & van der Walt, D. J. 2003, MNRAS, 339, L33
Haemmerlé, L., Eggenberger, P., Meynet, G., Maeder, A., & Charbonnel, C. 2016, A&A, 585, A65
Harris, C. R., Millman, K. J., van der Walt, S. J., et al. 2020, Natur, 585, 357
Hirota, T., Machida, M. N., Matsushita, Y., et al. 2017, NatAs, 1, 0146
Hirota, T., Wolak, P., Hunter, T. R., et al. 2022, PASJ, 74, 1234
Hosokawa, T., & Omukai, K. 2009, ApJ, 691, 823
Hunter, J. D. 2007, CSE, 9, 90
Hunter, T. R., Brogan, C. L., MacLeod, G., et al. 2017, ApJL, 837, L29
Hunter, T. R., Brogan, C. L., MacLeod, G. C., et al. 2018, ApJ, 854, 170
Inayoshi, K., Sugiyama, K., Hosokawa, T., Motogi, K., & Tanaka, K. E. I. 2013, ApJL, 769, L20
Jones, B. M., Fuller, G. A., Breen, S. L., et al. 2020, MNRAS, 493, 2015
Kondo, T., Koyama, Y., Ichikawa, R., et al. 2008, JGSJ, 54, 233 https://www.researchgate.net/publication/287498622_Development_of_the_K5VSSP_system
Kozyreva, A., Nakar, E., Waldman, R., Blinnikov, S., & Baklanov, P. 2020, MNRAS, 494, 3927
Lomb, N. R. 1976, Ap&SS, 39, 447
Mainzer, A., Bauer, J., Cutri, R. M., et al. 2014, ApJ, 792, 30
Maswanganye, J. P., Gaylard, M. J., Goedhart, S., Walt, D. J. v. d., & Booth, R. S. 2015, MNRAS, 446, 2730
Menten, K. M. 1991, ApJL, 380, L75
Meyer, D. M. A., Haemmerlé, L., & Vorobyov, E. I. 2019, MNRAS, 484, 2482
Moscadelli, L., Sanna, A., & Goddi, C. 2011, A&A, 536, A38
Motogi, K., Hirota, T., Machida, M. N., et al. 2019, ApJL, 877, L25
Motogi, K., Hirota, T., Sorai, K., et al. 2017, ApJ, 849, 23
Motogi, K., Sorai, K., Honma, M., et al. 2016, PASJ, 68, 69
Muñoz, D. J., & Lai, D. 2016, ApJ, 827, 43
Nakamura, M., Motogi, K., Nakamura, H., Yonekura, Y., & Fujisawa, K. 2023, MNRAS, 526, 1000
Neckel, T. 1978, A&A, 69, 51
NEOWISE Team. 2020, NEOWISE-R Single Exposure (L1b) Source Table, IPAC, doi:10.26131/IRSA144
Parfenov, S. Y., & Sobolev, A. M. 2014, MNRAS, 444, 620
Rajabi, F., Houde, M., MacLeod, G. C., et al. 2023, MNRAS, 526, 443
Rashidi, T., Anari, V., Bartkiewicz, A., et al. 2025, MNRAS, 542, L12
Sanna, A., Menten, K. M., Carrasco-González, C., et al. 2015, ApJL, 804, L2
Sanna, A., Moscadelli, L., Cesaroni, R., et al. 2010, A&A, 517, A78
Scargle, J. D. 1982, ApJ, 263, 835
Selina, R. J., Murphy, E. J., McKinnon, M., et al. 2018, ASPC, 517, 15
Song, S.-M., Chen, X., Liu, S.-Y., & Liu, J.-T. 2025, ApJ, 980, 132
Soszyński, I., Udalski, A., Szymański, M. K., et al. 2017, AcA, 67, 297
Stahler, S. W., Shu, F. H., & Taam, R. E. 1980a, ApJ, 242, 226
Stahler, S. W., Shu, F. H., & Taam, R. E. 1980b, ApJ, 241, 637
Sugiyama, K., Fujisawa, K., Doi, A., et al. 2014, A&A, 562, A82
Sugiyama, K., Saito, Y., Yonekura, Y., & Momose, M. 2019, ATel, 12446, 1
Szymczak, M., Durjasz, M., Goedhart, S., et al. 2024, A&A, 682, A17
Szymczak, M., Wolak, P., Bartkiewicz, A., & van Langevelde, H. J. 2011, A&A, 531, L3

Tanabe, Y., & Yonekura, Y. 2024, PASJ, 76, 426
Tanaka, K. E. I., Zhang, Y., & Motogi, K. 2021, arXiv:2103.08859
Uchiyama, M., Ichikawa, K., Sugiyama, K., Tanabe, Y., & Yonekura, Y. 2022, ApJ, 936, 31
Urquhart, J. S., Wells, M. R. A., Pillai, T., et al. 2022, MNRAS, 510, 3389
van der Walt, D. J. 2011, AJ, 141, 152
van der Walt, D. J., Maswanganye, J. P., Etoka, S., Goedhart, S., & van den Heever, S. P. 2016, A&A, 588, A47
Wolak, P., Szymczak, M., Kobak, A., et al. 2025, A&A, 701, A28
Yonekura, Y., Saito, Y., Sugiyama, K., et al. 2016, PASJ, 68, 74
Zhang, Y., Tan, J. C., Tanaka, K. E. I., et al. 2019, NatAs, 3, 517
Zinchenko, I. I., Salii, S. V., Sobolev, A. M., et al. 2025, MNRAS, 543, L9